Title	Experimental investigation of a multistage buckling-restrained brace
Authors	Ben Sitler, Toru Takeuchi, Ryota Matsui, Masao Terashima, Yuki Terazawa
Citation	Engineering Structures, Vol. 213, no. 110482,
Pub. date	2020, 6

Engineering Structures 213 (2020) 110482

Contents lists available at ScienceDirect

Engineering Structures

journal homepage: www.elsevier.com/locate/engstruct

Experimental investigation of a multistage buckling-restrained brace

Ben Sitler[a,*], Toru Takeuchi[a], Ryota Matsui[b], Masao Terashima[c], Yuki Terazawa[a]

[a] Tokyo Institute of Technology, Tokyo, Japan
[b] Hokkaido University, Sapporo, Japan
[c] Nippon Steel Engineering, Tokyo, Japan

ARTICLE INFO

Keywords:
Buckling-restrained brace
Multistage
Low yield point steel
High strength steel
Residual drift

ABSTRACT

While buckling-restrained braces offer excellent energy dissipation characteristics, their low post-yield stiffness may result in large residual drifts and interstory drift concentration when used in simply supported frames. This paper introduces a new multistage buckling-restrained brace to help mitigate these design challenges. The proposed device features two low yield point (LYP) cores with LY225 and short yield lengths, and one high yield point (HYP) core with SA440B and a longer yield length. In a design level event, the LYP cores dissipate energy, while the parallel HYP core provides an elastic restoring force. At large drifts, the HYP core yields and the device acts similar to a high-capacity, ductile, conventional BRB.

A 384 kN specimen was tested at up to 1.5% strain and the individual core contributions recorded using strain gauges attached to the elastic core segments inside the restrainer. The multistage response matched the predicted trilinear backbone, achieving 10 to 20% equivalent damping prior to yielding the HYP core, and a fatigue capacity exceeding three times the AISC 341-16 acceptance criteria. Interaction between the decoupled cores was studied using a 3D finite element model, indicating that minor detailing changes could further improve performance.

1. Introduction

Buckling-restrained braces (BRBs) are widely used as the primary ductile members in seismic lateral force resisting systems [1]. BRBs employ axially decoupled restrainers to limit the core higher-mode buckling amplitude, producing balanced compressive and tension strengths that enable engineers to tune the capacity to match the seismic demand. However, in simply supported BRB frames (BRBFs), this results in a pushover curve with low post-yield stiffness, which is essentially limited to strain hardening of the core. Low post-yield stiffness limits the ability of BRBFs to distribute interstory drifts along the structure height [2], produces large residual drifts [3] and increases the collapse probability under severe ground motions [3]. Conversely, engineers seeking better performance may choose to oversize the BRBs, following the maxim that “ductility equals damage.” However, well-designed BRBs do not show visible damage and possess significant excess fatigue capacity, while increasing the strength amplifies floor accelerations, potentially increasing the nonstructural damage in acceleration-sensitive components during moderate events.

Existing solutions to address these design challenges include dual moment frames [4] with short BRBs [5], spine frames [6], self-centering BRBs [7] and BRBs with supplementary dampers [8] (refer to [1] for a comprehensive review). However, these systems and devices require additional structural components, imposing significant costs over a simply supported frame with conventional BRBs. This paper proposes a new multistage buckling-restrained brace (MS-BRB) to reduce residual drift and interstory drift concentration. The proposed device employs similar fabrication and design methods, and features a similar composition as conventional BRBs, which are useful characteristics for practical application. This paper briefly introduces the proposed device and equations describing the trilinear backbone curve, and then presents a detailed experimental and numerical study characterizing the device behavior and multistage response.

1.1. Multi-material buckling-restrained brace concept

One approach to achieving multistage behavior with BRBs is to provide parallel low yield point (LYP) and high yield point (HYP) cores that yield at different drifts. In moderate earthquakes, the LYP core yields and dissipates energy, slightly reducing floor accelerations, while the HYP core provides an elastic restoring force, reducing residual drifts and improving the post-earthquake repair/replace decision. At large drifts, where transient drifts and collapse are the primary concerns, the HYP core yields and the device behaves similar to a high-capacity,

---

* Corresponding author.
E-mail address: sitler.b.aa@m.titech.ac.jp (B. Sitler).

https://doi.org/10.1016/j.engstruct.2020.110482
Received 15 October 2019; Received in revised form 5 March 2020; Accepted 6 March 2020

ductile, conventional BRB. In a simply supported frame, this effectively modifies the story hysteresis from a bilinear curve with low post-yield stiffness to a trilinear curve reminiscent of a dual BRB-moment frame, albeit with a slightly smaller second stage yield drift.

This basic concept was originally proposed by Saeki [9], who tested a multi-material BRB in the 1990s. Recently, researchers [10–13] have numerically investigated this concept for simply supported BRBFs and reported substantial residual drift reduction. However, these studies have relied upon extremely low yield (e.g., LY100, $80 \le f_y \le 120$ MPa) and high strength (e.g., WT780/HPS100W, $f_y > 700$ MPa) steel grades. LY100 exhibits severe isotropic hardening, dramatically increasing the connection and column forces, with the AIJ Recommendations suggesting a strain hardening overstrength factor of $\omega = 2.7$ (§3.2.2 [14]). Isotropic hardening also diminishes the multistage effect, which has been shown to be more effective in reducing residual drifts than increasing the brace overstrength [15]. Meanwhile, WT780 has a low material overstrength ($f_y/f_u \approx 0.9$) and ultimate strain ($\varepsilon_u < 10\%$), which may adversely affect the core higher-mode buckling response and local strain demands. Thus, using a narrower range of steel grades to achieve the multistage effect is preferable.

Other multistage concepts have also been proposed, either attaching a sacrificial hysteretic damper [16] to the restrainer or placing multiple cores in series with a lockup mechanism [17]. However, these compositions impose other tradeoffs and are outside the scope of this discussion.

1.2. Proposed multistage buckling-restrained brace

This paper introduces the MS-BRB composition shown in Fig. 1. The innovation over previous proposals is to manipulate the strain demands by varying the core yield lengths, which is achieved by only welding the cores together at the connections, decoupling the LYP and HYP core strains along the core yield lengths. Two LYP cores with a lower steel grade (i.e., smaller yield strain) and shorter yield length (i.e., higher strain demand) sandwich a HYP core with a higher steel grade (i.e., larger yield strain) and longer yield length (i.e., lower strain demand). A significant multistage effect may then be achieved using steel grades with better strain hardening, overstrength and ductility characteristics (e.g., LY225 and SA440B), while reducing the dependence on the precise material strength, which varies and is generally not known until the steel plate is delivered.

This study adopts LY225 for the LYP cores, as this is one of the three standard materials used for BRBs in Japan (others being SN400B and SN490B) [18] and offers a low yield strength ($205 \le f_y \le 245$ MPa), moderate overstrength ($\omega = 1.35$, §3.2.2 [14]) and negligible isotropic hardening. The HYP core employs SA440B, a ductile, high-strength steel with a specified overstrength ($f_u / f_y \ge 1.25$) and elongation at fracture ($\varepsilon_f \ge 20\%$) almost identical to SN400B and SN490B. While the yield strength of SA440B ($440 \le f_y \le 540$ MPa) exceeds the maximum typically permitted in seismic members (e.g., $f_y \le 345$ MPa, §A3.1 [19]), BRBs are qualified through physical testing, an exception to this prescriptive criteria (§A3.1 [19]). While LY225 and SA440B are used in this experiment, other material combinations (e.g., A36 and HPS70W) may also be feasible.

2. Trilinear backbone curve

This section presents simple equations to describe the trilinear backbone shown in Fig. 1 for a MS-BRB with cores of different yield lengths and steel grades. First, the gross yield strength (N_y) (Eq. (1)) is calculated as the sum of the LYP and HYP core yield strengths ($f_{y,L}$, $f_{y,H}$) multiplied by the yield areas ($A_{y,L}$, $A_{y,H}$), which are identified in Fig. 2. Note that the subscripts L and H denote the respective LYP and HYP core quantities.

$$N_y = f_{y,L}A_{y,L} + f_{y,H}A_{y,H} \tag{1}$$

The force at which the LYP cores yield ($N_{y,L}$) is given by Eq. (2). As the stress in the elastic HYP core is less than $f_{y,L}$ due to its longer yield length, it is necessary to apply an effective area factor (α) (Eq. (3a)) when calculating the first yield force from the total yield area (A_y) (Eq. (3b)). This factor depends on the core stiffness modification factors (KF_L, KF_H) given by Eqs. (4a) and (4b), while the core yield lengths ($L_{y,L}$, $L_{y,H}$), elastic areas ($A_{e,L}$, $A_{e,H}$), yield areas ($A_{y,L}$, $A_{y,H}$) and decoupled length (L_{core}) are depicted in Fig. 2.

$$N_{y,L} = f_{y,L}\cdot\alpha A_y \tag{2}$$

where,

$$\alpha = \frac{1 + A_{y,H}/A_{y,L}\cdot KF_H/KF_L}{1 + A_{y,H}/A_{y,L}}, \tag{3a}$$

$$A_y = A_{y,L} + A_{y,H} \tag{3b}$$

$$KF_L = \left(\frac{L_{y,L}}{L_{core}} + \frac{A_{y,L}}{A_{e,L}} - \frac{L_{y,L}}{L_{core}}\frac{A_{y,L}}{A_{e,L}}\right)^{-1}, \tag{4a}$$

$$KF_H = \left(\frac{L_{y,H}}{L_{core}} + \frac{A_{y,H}}{A_{e,H}} - \frac{L_{y,H}}{L_{core}}\frac{A_{y,H}}{A_{e,H}}\right)^{-1} \tag{4b}$$

The elastic brace stiffness (K) (Eq. (5)) is then be calculated from the Young's modulus (E) (assumed equal for all cores), total yield area (A_y), workpoint length (L_{wp}) and workpoint stiffness modification factor (KF) (Eq. (6)), where A_e is the connection area. Note that the long HYP core moderates the increase in stiffness resulting from the short LYP core yield length, which is accounted for by the αKF_L term. The high strength steel used for the HYP core will also reduce the required area A_y, and so MS-BRBs should only be slightly stiffer than conventional BRBs with yield lengths equal to L_{core}, even if the KF factor is larger.

$$K = \frac{KF\cdot EA_y}{L_{wp}} \tag{5}$$

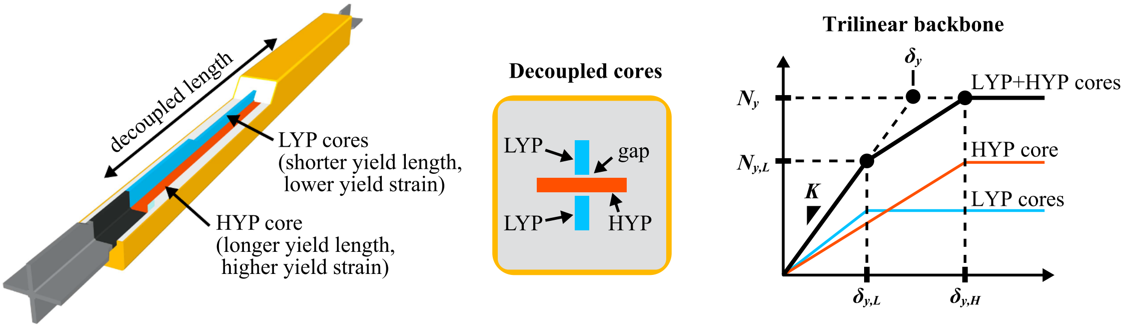

Fig. 1. Multistage buckling-restrained brace concept.

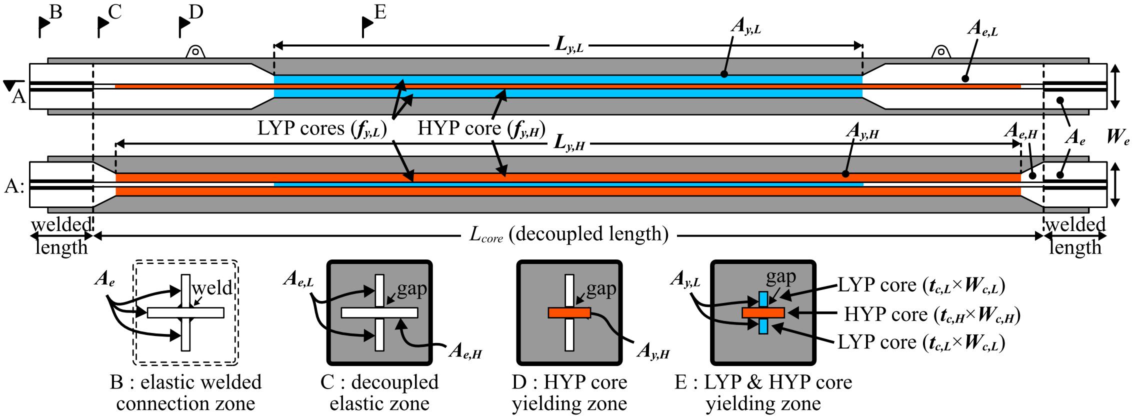

Fig. 2. Core dimensions.

$$KF = \left(\frac{L_{core}}{L_{wp}}\cdot\frac{1}{\alpha KF_L} + \frac{A_y}{A_e} - \frac{L_{core}}{L_{wp}}\frac{A_y}{A_e}\right)^{-1} \tag{6}$$

While the first yield displacement ($\delta_{y,L}$) is given by Eq. (7), it is useful to define an effective yield displacement δ_y (Eq. (8)), which is equal to that of a bilinear device with stiffness K and capacity N_y.

$$\delta_{y,L} = \frac{N_{y,L}}{K} \tag{7}$$

$$\delta_y = \frac{N_y}{K} \tag{8}$$

Finally, the HYP yield displacement ($\delta_{y,H}$) may be obtained from the yield drift ratio ($\delta_{y,H}/\delta_{y,L}$) given by Eq. (9a). In the typical case of $L_{y,H}/L_{wp} > 0.8$, this further simplifies to Eq. (9b), which equals 0.95–1.0 times Eq. (9a) due to the small value of the coefficient κ. Note that Eqs. (9a) and (9b) assume that Young's modulus is similar for all cores.

$$\frac{\delta_{y,H}}{\delta_{y,L}} = \frac{f_{y,H}}{f_{y,L}}\frac{KF_L}{KF_H}\cdot\frac{1+\frac{KF_H}{KF_L}\frac{f_{y,L}}{f_{y,H}}\frac{N_y}{N_{y,L}}\cdot\kappa}{1+\kappa},$$
$$\text{where}\quad \kappa = \frac{A_{y,L}KF_L + A_{y,H}KF_H}{A_e}\left(\frac{L_{wp}}{L_{core}} - 1\right) \tag{9a}$$

$$\frac{\delta_{y,H}}{\delta_{y,L}} \approx \frac{f_{y,H}}{f_{y,L}}\frac{KF_L}{KF_H}\ \left(\text{for } \frac{L_{y,H}}{L_{wp}}, \frac{L_{core}}{L_{wp}} > 0.8\right) \tag{9b}$$

These parameters (N_y, $N_{y,L}$, K, KF, $\delta_{y,L}$, δ_y, $\delta_{y,H}$) are calculated for the test specimen in Section 3.1.

3. Experiment

Previous numerical studies have noted that multistage BRBs significantly reduce residual drift [15], but there have been few tests to confirm the seismic performance of the unique core designs required for the trilinear hysteresis. Therefore, a cyclic displacement-controlled test was conducted to investigate the performance of the unique core configuration and validate the trilinear backbone developed in Section 2.

3.1. Test setup

A small-scale specimen with a $N_y = 384$ kN gross yield strength was tested, as shown in Fig. 3. The core configuration features three rectangular plates arranged in a cruciform shape and welded together only at the ends, but left separated along the middle length $L_{core} = 2890$ mm. A pinned diagonal configuration inclined at a $\theta = 27.6^\circ$ brace angle was adopted to maximize the actuator capacity. As bulging is a concern for rectangular cores [1], a mortar-filled steel tube square restrainer was used to test an onerous case.

Instrumentation was provided to record the brace and core axial demands. The axial displacement (δ_{BRB}) was obtained from lasers attached to each end of the restrainer, while the axial brace force (N_{BRB}) was obtained from a load cell placed in series. Eight protected strain gauges were attached to the long elastic segments of the LYP cores, inside the mortar-filled restrainer and at least two plate widths from the nearest taper or weld, in order to estimate the individual core forces. One pair remained intact through the first three fatigue cycles.

The specimen (Fig. 3) featured two 16 × 20 mm LYP225 low yield point (LYP) cores, each with a yield length ratio of $L_{y,L} / L_{wp} = 0.44$. These sandwiched a single 19 × 30 mm SA440B high yield point core (HYP) core with a yield length ratio of $L_{y,H}/L_{wp} = 0.58$, which is shorter than typical full-scale BRBs. The cores were sized targeting a yield force ratio of $N_{y,L}/N_y \approx 0.6$, considering the limited actuator capacity and a minimum plate thickness of 16 mm. The core plates were wrapped individually with a 1 mm thick debonding material and then encased in a mortar-filled SHS restrainer (200 × 6 mm, STKR400), which was connected axially by a midspan shear key. Note that the delivered LYP225 plate was close to the average specified yield strength, while the SA440B plate only met the minimum specified strength during the high-speed mill certificate testing and not the quasi-static coupon tests. Furthermore, while the LY225 coupon tests shown in Fig. 4 are almost bilinear, SA440B did not exhibit a well-defined yield point, which was instead determined by intersecting the line drawn through a 0.2% strain offset and parallel to the elastic modulus. The mortar achieved a 28-day cylinder strength of $f_{ck} = 44$ MPa, while the core dimensions, material properties and yield points are summarized in Tables 1–3.

The loading protocol was specified in terms of the average axial strain of the LYP cores ($\varepsilon_L = \delta_{BRB}/L_{y,L}$), which is 33% greater than the average axial strain of the HYP core ($\varepsilon_H = \delta_{BRB}/L_{y,H}$) due to the different yield lengths. First, an ascending protocol was applied that consists of 2 cycles each at $\varepsilon_L = 0.1\%$, 0.2%, 0.4%, 0.7% and 1.5%. These amplitudes were selected to investigate the behavior just before and immediately after each core yields. The brace was then returned to the origin ($\delta_{BRB} = N_{BRB} = 0$) before applying a constant-amplitude fatigue protocol that targeted $\varepsilon_L = 1.5\%$ until fracture. Note that the fatigue cycles are numbered starting at the first ascending cycle at $\varepsilon_L = 1.5\%$, and the actual amplitudes varied from $\varepsilon_L = 1.4$ to 1.6%, limited by the actuator capacity and the strain hardened force. Additionally, slightly greater compressive displacements were applied during the first part of the ascending protocol until the yield points could be clearly identified. Key observations and cycles where each core first experienced significant yielding are indicated in Fig. 5.

3.2. Experimental results

The brace force-displacement and core stress–strain hysteresis are shown in Fig. 6 for the ascending protocol. Note that the yield length

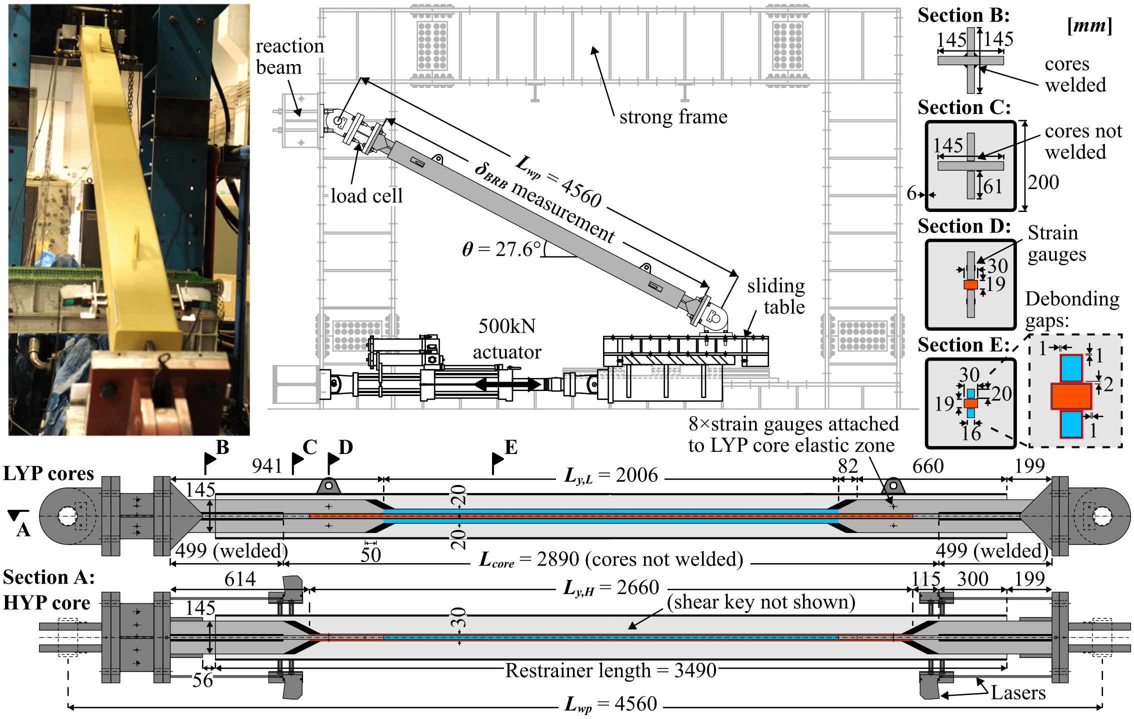

Fig. 3. Specimen and test setup.

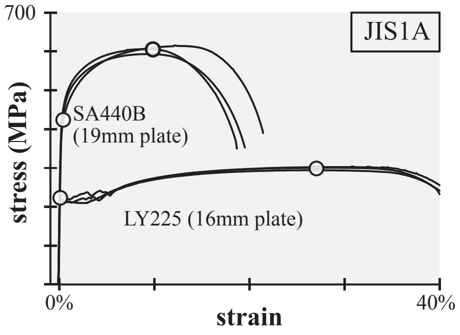

Fig. 4. Coupon tests.

ratio ($L_{y,L}/L_{wp}$ = 0.44) and brace angle (θ = 27.6°) result in a story drift angle of approximately 1.2 times the LYP core strain [1].

3.2.1. Response during ascending protocol

At small strains (ε_L = 0.1%, 0.2% and 0.4%), the brace hysteresis was bilinear with a steep post-yield stiffness. The multistage behavior was evident, as the LYP cores experienced moderate yielding, while the HYP core remained elastic. Although the area of the LYP cores (640 mm^2) slightly exceeds the HYP core area (570 mm^2), the elastic restoring force of the HYP core is greater than the yield strength of the LYP cores due to the larger yield strength of SA440B.

At moderate strains (ε_L = 0.7%), the brace hysteresis was trilinear and closely matched the predicted backbone curve defined in Table 3. The LYP cores exhibited a nearly bilinear hysteresis with a small Bauschinger effect, and the incremental force developed by the elastic HYP

Table 2
Material properties.

Steel Grade	E GPA	f_y MPa	ε_y %	f_u MPa	ε_u %	ε_f %
LYP225*	205	223	0.10%	299	27%	42%
SA440B*	200	424†	0.41%†	605	10%	20%
STKR400**	205	397	–	475	–	33%

*quasi-static coupon tests **mill certificate †0.2% strain offset.

Table 3
Trilinear backbone parameters.

N_y kN	$N_{y,L}$ kN	K kN/mm	KF –	$\delta_{y,L}$ mm	$\delta_{y,H}$ mm	$\delta_{y,H}/\delta_{y,L}$ –	δ_y mm
384	251	87	1.6	2.9	6.3	2.2	4.5

Table 1
Core dimensions.

Component	Grade	$t_{c,L} \times W_{c,L}$, $t_{c,H} \times W_{c,H}$	$A_{e,L}$, $A_{e,H}$	$L_{y,L}$, $L_{y,H}$	$A_{e,L}/A_{y,L}$ $A_{e,H}/A_{y,H}$	$L_{y,L}/L_{wp}$, $L_{y,H}/L_{wp}$	$L_{y,L}/L_{core}$, $L_{y,H}/L_{core}$
	–	mm	mm^2	mm	–	–	–
LYP cores	LYP225	2 × 16 × 20	1952	2006	3.1	0.44	0.70
HYP core	SA440B	19 × 30	2755	2660	4.8	0.58	0.92
	$t_e \times W_e$ mm		A_e mm^2	A_e/A_y –	L_{core} mm	L_{wp} mm	L_{core}/L_{wp} –
Connections	19 × 145 + 2 × 16 × 63		4771	3.9	2890	4560	0.63

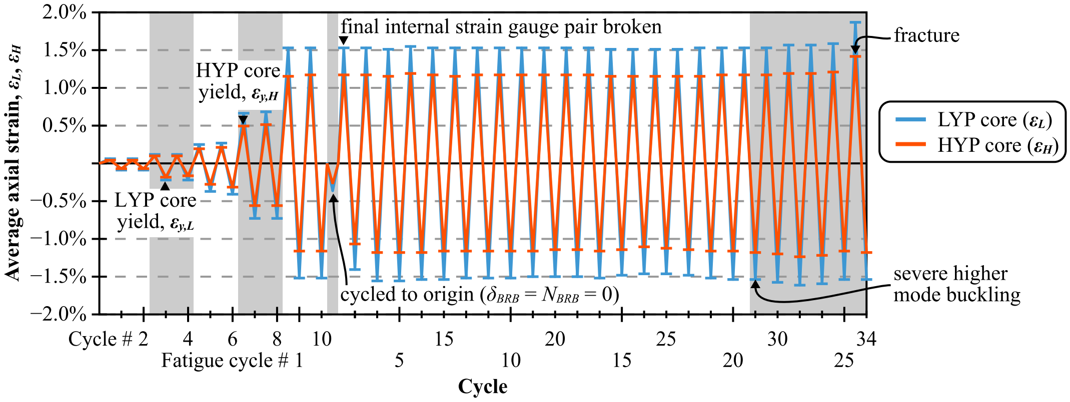

Fig. 5. Loading Protocol.

core dominated the brace post-yield stiffness, rather than kinematic hardening of the LYP cores. Although SA440B does not have a well-defined yield point, the nominal HYP core yield strength was reached at a displacement corresponding to a 0.2% strain offset.

At design level strains (ε_L = 1.5%), which correspond to a displacement ductility of δ_{BRB}/δ_y = 7 (or $\delta_{BRB}/\delta_{y,L}$ = 10), the brace hysteresis resembled a conventional BRB with an enhanced Bauschinger effect. The HYP core developed about 60% of its potential strain hardening, resulting in a compressive overstrength of $\beta\omega$ = 1.3 and maxing out the actuator capacity. The large kinematic hardening of SA440B provided a post-yield stiffness of about 0.04 times the initial elastic stiffness. Note that almost all of the internal strain gauges broke during these cycles, with the final pair breaking at the start of the fatigue protocol (third cycle at ε_L = 1.5%).

The difference between the HYP (N_{HYP}) and LYP (N_{LYP}) core forces is shown in Fig. 7, with three key points labelled Points A, B and C. At peak displacements (Point A), the force difference reached $N_{HYP} - N_{LYP}$ ≈ 115 kN, exceeding the difference in core yield strengths ($f_{y,H}A_{y,H} - f_{y,L}A_{y,L}$ = 99 kN) by 15% due to increased rate of strain hardening in SA440B compared to LY225. After fully yielding and unloading the device (Point B), equal and opposite residual forces equal to $N_{resid} \approx \pm$ 74 kN (19% N_y) were present in the cores due to the greater unloading displacement of the HYP core. After returning to the origin (δ_{BRB} = N_{BRB} = 0, i.e., no residual drift) (Point C), a small residual force of $N_{resid} \approx \pm$ 22 kN (6% N_y) was still present, bounding the potential residual core forces.

While these residual forces are resolved internally in the proposed device, future researchers may consider placing the LYP and HYP cores in separate BRBs. However, in that case, permanent transfer forces equal to N_{resid} should be included in the non-seismic load combinations when designing the frame, given that yielding may occur multiple times throughout the building's design life. Eq. (10) gives a conservative upper bound estimate of N_{resid}, corresponding to the HYP core yielding and then immediately unloading (Point B).

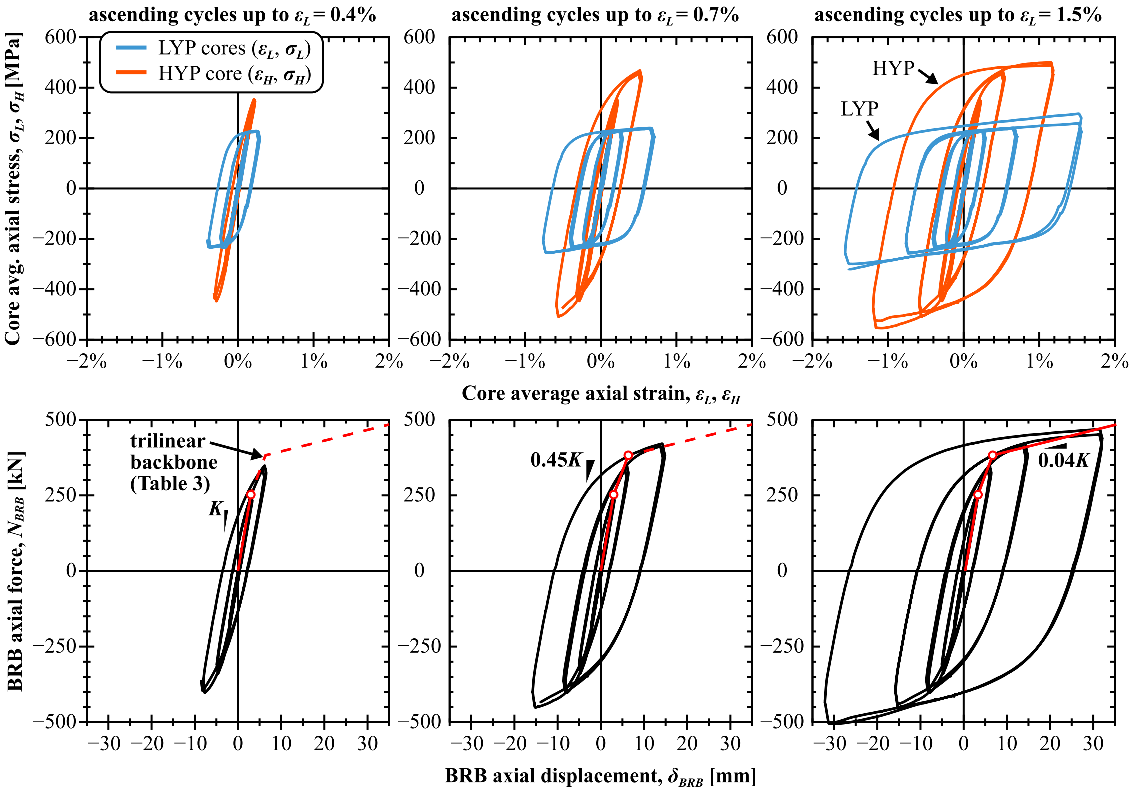

Fig. 6. Hysteresis during ascending protocol.

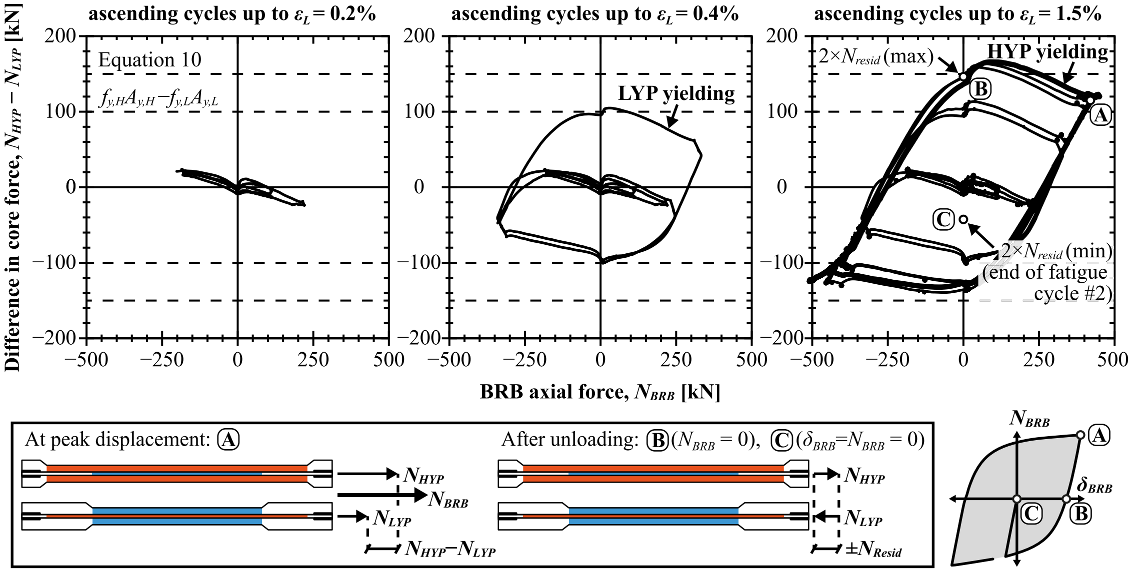

Fig. 7. Difference in core force.

$$N_{resid} = \frac{\omega f_{y,H} A_{y,H}}{2}\left(1 - \frac{\delta_{y,L}}{\delta_{y,H}}\right) \tag{10}$$

3.2.2. *Response during fatigue protocol*

Fatigue cycles were then applied at the maximum strain amplitude ($\varepsilon_L = 1.5\%$) until failure, resulting in the brace force-displacement response shown in Fig. 8. Note that Fig. 8 starts at the third fatigue cycle, as the first two cycles at $\varepsilon_L = 1.5\%$ were already included in the ascending protocol results (Fig. 6).

The force envelope remained stable for the first 20 fatigue cycles, but the hysteresis then gradually developed a pinched shape, particularly on the compressive side. The compressive strength retained at least 85% of the envelop strength until fatigue cycle #21, at which point pinching became more pronounced, indicating large-amplitude ("severe") higher-mode buckling. The HYP core fractured during the tensile portion of fatigue cycle #26 and was immediately followed by one of the LYP core plates. A compression half-cycle was applied before terminating the test, with the final LYP core plate fracturing during the specimen deconstruction (Section 3.2.6). Slight bulges were observed on the top and bottom of the restrainer's upper end during the post-test inspection. These were not visible in the video recording nor earlier inspections, and there was no indication of instability in the axial hysteresis, which suggests that they developed during the post-fracture compressive half-cycle.

3.2.3. *Compressive overstrength*

The compressive overstrength factor (β) is the ratio of the maximum compression and tension forces over a single, stabilized and symmetric cycle ($\beta = |N_{BRB}{}^{-}/N_{BRB}{}^{+}|$). While BRBs develop greater forces in compression due to Poisson expansion, higher-mode buckling and friction, β should be kept below 1.2 [1], or 1.5 according to AISC 341–16 (§K3.8 [19]). Fig. 9a indicates that the compressive overstrength factor remained stable at $\beta = 1.06$ throughout the fatigue cycles ($\varepsilon_L = 1.5\%$), but fell slightly below 1.0 ($\beta = 0.99$ and 0.96) during the first four cycles at $\varepsilon_L = 0.1$ and 0.2%. Values less than $\beta < 1.0$ are characteristic of BRBs with large debonding gaps (typically greater than 0.1 times the core thickness per face), as the higher-mode buckling geometry accounts for a small component of the axial deformation, reducing the axial stresses when in compression. This phenomenon is depicted schematically in Fig. 9b. As large debonding gaps increase the thrust and friction at large strains, this phenomenon can produce a pinched hysteresis. However, despite this pinching behavior, β remained constant through all but the final fatigue cycles (Fig. 9a).

3.2.4. *Energy dissipation*

The single-cycle equivalent damping ratios (ξ_{eq}, $\xi_{eq,L}$, $\xi_{eq,H}$) were calculated from the hysteretic ($E_{h,L}$, $E_{h,H}$) and strain ($E_{s,L}$, $E_{s,H}$) energies of each core [20] following Eqs. (11a)–(11c). These are shown in Fig. 10a, and the proportion of hysteretic energy dissipated by the LYP cores in Fig. 10b. An overall equivalent damping ratio of $\xi_{eq} = 10\%$ was

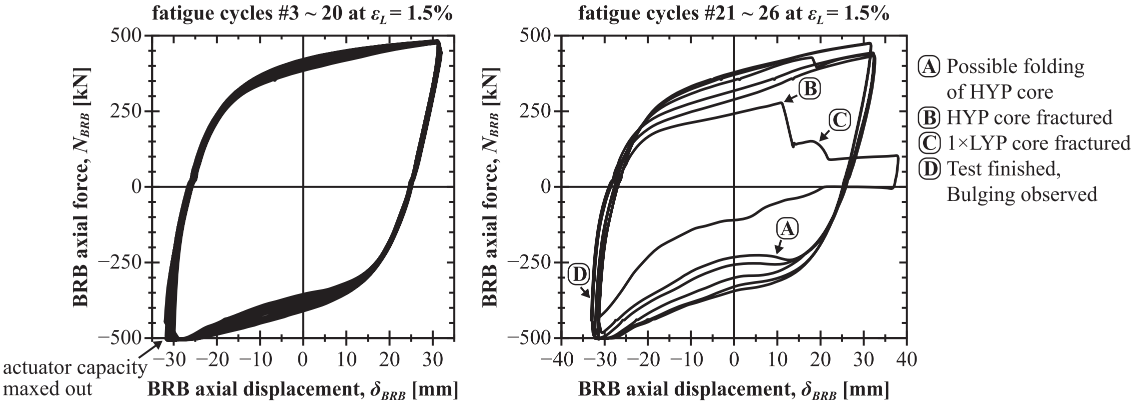

Fig. 8. Hysteresis during fatigue protocol.

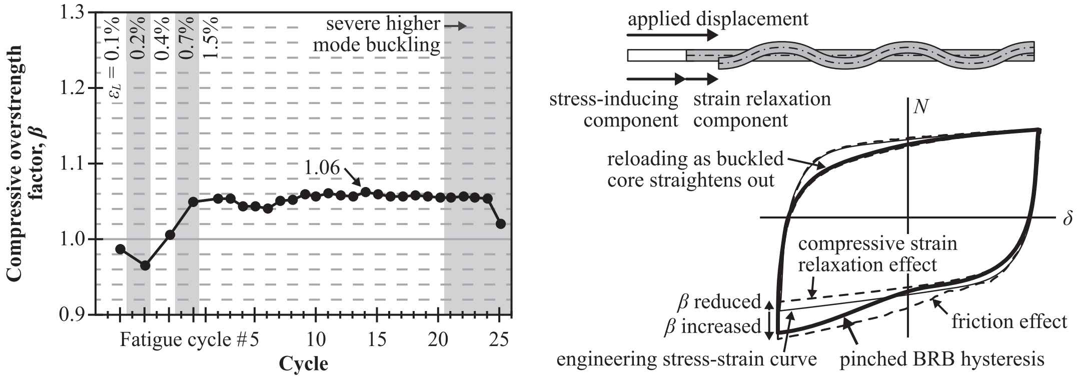

a) Compressive overstrength factor

b) Compressive strain relaxation

Fig. 9. Compressive overstrength.

achieved once the LYP cores yielded ($\varepsilon_L = 0.2\%$), and subsequently increased to $\xi_{eq} = 20\%$ at $\varepsilon_L = 0.4\%$, with the LYP cores dissipating 68% of the hysteretic energy. Although the HYP core was nominally elastic at this stage, there was some inelasticity as SA440B lacks a well-defined yield point. Finally, the equivalent damping increased to $\xi_{eq} = 42\%$ at $\varepsilon_L = 1.5\%$, with the ratio of hysteretic energy dissipated by the LYP cores converging to their contribution to the gross yield strength ($f_{y,L}A_{y,L}/N_y = 37\%$).

$$\xi_{eq} = \frac{E_{h,L} + E_{h,H}}{4\pi(E_{s,L} + E_{s,H})}, \tag{11a}$$

$$\xi_{eq,L} = \frac{E_{h,L}}{4\pi E_{s,L}}, \tag{11b}$$

$$\xi_{eq,H} = \frac{E_{h,H}}{4\pi E_{s,H}} \tag{11c}$$

where the core hysteretic energies are $E_{h,L} = \int N_{LYP}\delta_{BRB}$ (LYP cores) and $E_{h,H} = \int N_{HYP}\delta_{BRB}$ (HYP core), and the core strain energies are $E_{s,L} = 0.5N_{LYP}\delta_{BRB}$ (LYP cores) and $E_{s,H} = 0.5N_{HYP}\delta_{BRB}$ (HYP core).

3.2.5. *Fatigue*

While ultra-low cycle fatigue is often the mechanism of fracture during earthquakes, it is a nonlinear function of the local stress and strain state. Instead, the fatigue performance of BRBs is typically compared using empirical low cycle fatigue (*LCF*) curves or cumulative inelastic deformation (*CID*), as these only require the global deformations. Both measures are useful in specific contexts: *LCF* damage (D_{LCF}) has been used to estimate the residual capacity after real earthquakes (e.g., 2011 Great East Japan Earthquake [1]), while AISC 341–16 requires qualification specimens to achieve $CID > 200$ in a standard loading protocol (e.g., §K3.4c [19]).

D_{LCF} (Eq. (12a)) is defined as the cumulative number of cycles (N) divided by the cycles to fracture (N_f) for each strain range ($\Delta\varepsilon = \Delta\varepsilon_L$ or $\Delta\varepsilon_H$, where $\Delta\varepsilon_L = (|\delta_{BRB}^-| + \delta_{BRB}^+)/L_{y,L}$, $\Delta\varepsilon_H = (|\delta_{BRB}^-| + \delta_{BRB}^+)/L_{y,H}$). This requires a supplier-specific Coffin-Manson curve [21] (Eq. (12b)), which will be lower than that of the base material due to local effects such as higher-mode buckling, fabrication imperfections and strain concentration.

CID is the cumulative inelastic axial deformation normalized by the workpoint yield displacement. However, this will vary with the selected loading protocol and yield displacement, and so two values are provided. First, CID_{LYP} (Eq. (13)) is calculated directly from the recorded workpoint displacements and LYP yield displacement ($\delta_{y,L} = 2.9$ mm), excluding pin slip. Second, CID_{AISC} (Eq. (14)) is calculated from adjusted strains matched to the AISC 341-16 drift protocol and the effective yield displacement ($\delta_y = 4.5$ mm). Drift is taken as equal to ε_L, corresponding to potential project conditions of $\theta = 45°$ and $L_{y,L}/L_{wp} = 0.5$, and then adjusted using a Coffin-Manson exponent of 0.49 to the target protocol of 2 × 0.5%, 2 × 1.0%, 2 × 1.5%, 2 × 2.0% and 22 × 1.5% drift (§K3.4c [19]). Of the 26 fatigue cycles, which account for 97% of the LCF damage, the accumulated CID_{AISC} capacity was reduced by −44% for two cycles (targeting 2% drift), while no adjustment was applied for the remaining fatigue cycles (targeting 1.5% drift).

$$D_{LCF} = \sum \frac{N}{N_f}, \text{ where } \quad N_f = \left(\frac{\Delta\varepsilon}{0.2048}\right)^{-1/0.49} \tag{12a,b}$$

$$CID_{LYP} = \sum 4\frac{\delta_{BRB} - \delta_{y,L}}{\delta_{y,L}} \tag{13}$$

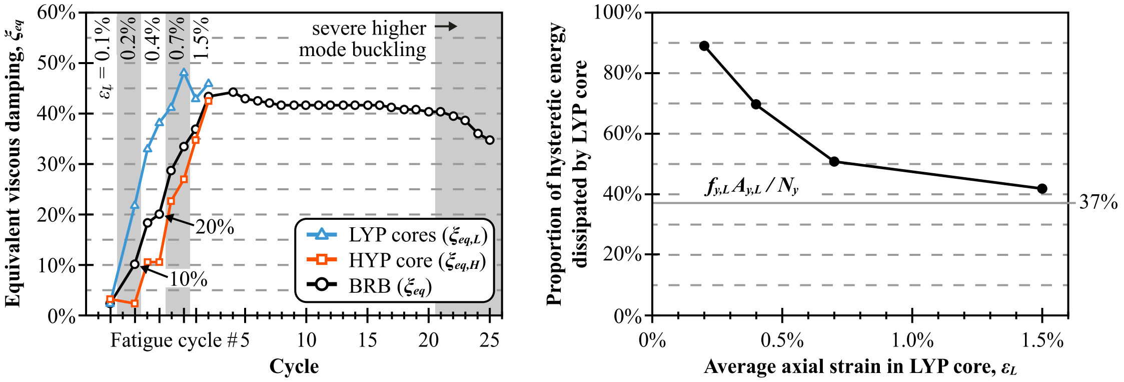

a) Equivalent viscous damping

b) Hysteretic energy dissipation

Fig. 10. Energy dissipation.

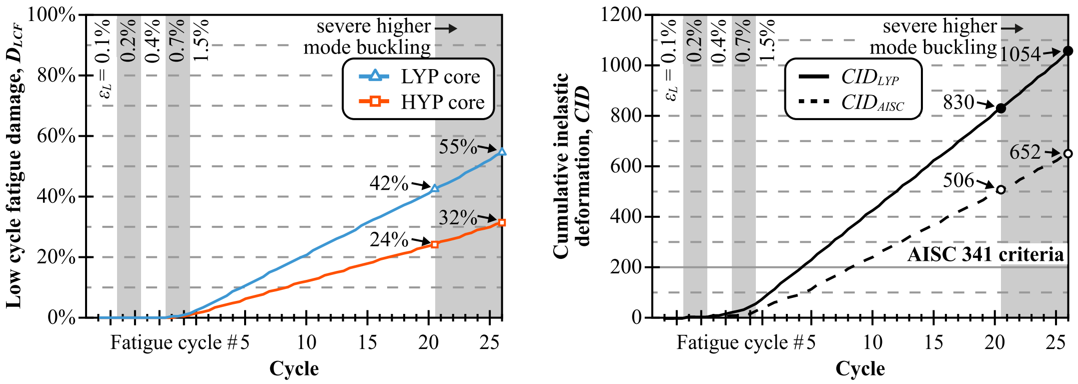

a) Low cycle fatigue damage

b) Cumulative inelastic deformation

Fig. 11. Fatigue performance.

$$CID_{AISC} = \sum 4\frac{\delta_{BRB}-\delta_y}{\delta_y}\cdot\left(\frac{\Delta\varepsilon_{L,Test}}{\Delta\varepsilon_{L,Target}}\right)^{1/0.49} \tag{14}$$

The LCF damage for each core and two *CID* capacities are shown in Fig. 11. The AISC 341-16 acceptance criteria of $CID > 200$ (§K3.4c [19]) was significantly exceeded (Fig. 11b), with the specimen achieving $CID_{LYP} = 1054$ or $CID_{AISC} = 652$, depending on how the yield displacement is defined and target loading protocol. However, the LCF damage (Fig. 11a) of the LYP cores was only $D_{LCF} = 55\%$ at fracture. This suggests that the fatigue capacity is adequate for several design level events, but that the device did not perform as well as conventional BRBs produced by that supplier. This is logical, as well-designed BRBs typically have fatigue capacities well in excess of minimum code requirements, and this test specimen experienced a premature fracture due to severe higher-mode buckling, which is investigated further in Section 4.

3.2.6. Specimen deconstruction

The deconstructed specimen is shown in Fig. 12. Mortar cracking was observed at both ends of the LYP yield length, which is indicative of bulging, even if this did not result in a loss of compressive strength or instability. The HYP weak axis higher-mode buckling amplitude exceeded the as-built debonding gap due to mortar crushing, while the LYP strong axis amplitude was slightly smaller due loose mortar grains filling in between the LYP and HYP cores. Also, the plastic higher-mode buckling wavelengths of the LYP and HYP cores were nearly equal, averaging about 180 mm along the core length, including the flat wavecrest widths. This is notable, as current theory [1] suggests that the average LYP strong axis ($W_{c,L} = 20$ mm) wavelength should be 45% longer than the average HYP weak axis ($t_{c,H} = 19$ mm) wavelength due to the large difference in steel grades.

4. Numerical model

4.1. Modelling assumptions

To investigate the higher-mode buckling response and core interaction, a detailed 3D finite element model was constructed and analyzed using Abaqus/Explicit [22]. Quasi-static explicit analysis is well suited to highly nonlinear problems, as implicit solvers struggle to converge with the large plastic strains, intermittent sliding contact and snap-through buckling experienced by BRB cores. The explicit solver with a loading rate of 400 mm/s (minimum element length of 6 mm) gave strains and reactions nearly identical to the implicit results.

The core, mortar and restrainer are shown in Fig. 13 and were modelled using linear reduced integration (C3D8R) elements. Following a mesh sensitivity study, the core was subdivided to $t_c / 3$ across the thickness and $t_c / 2$ along the length, which gives at least 4 elements along each half wavelength. The 1 mm debonding gaps were directly modelled, and General Contact with a friction coefficient of $\mu = 0.2$ was selected based on trial and error, although a lower coefficient may be justified, as $\mu = 0.1$ gave similar results. Contact with $\mu = 0.3$ was assigned between the mortar and steel restrainer to capture the partial composite action.

The elastic core segments and steel tube restrainer adopted trilinear kinematic hardening models based on the yield and ultimate points (f_y,

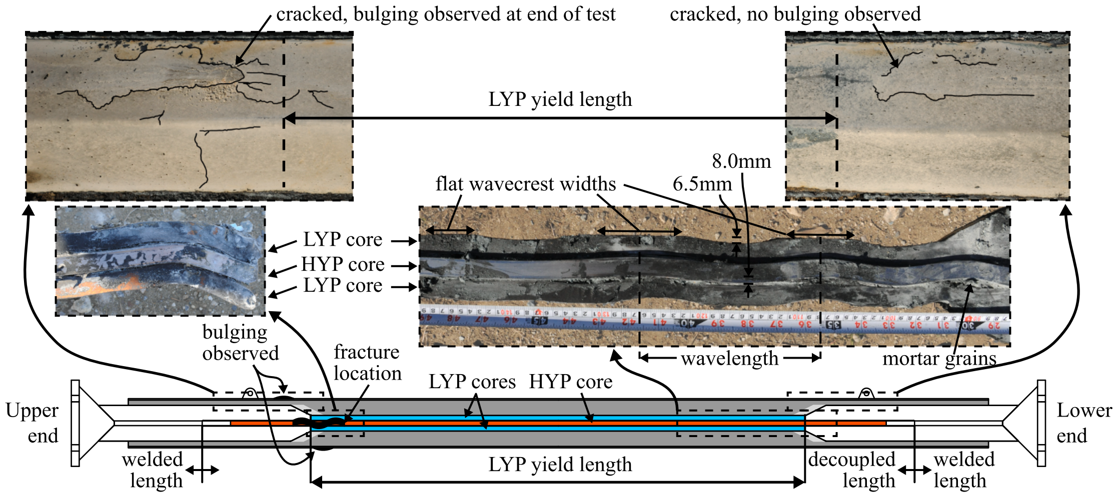

Fig. 12. Deconstructed specimen.

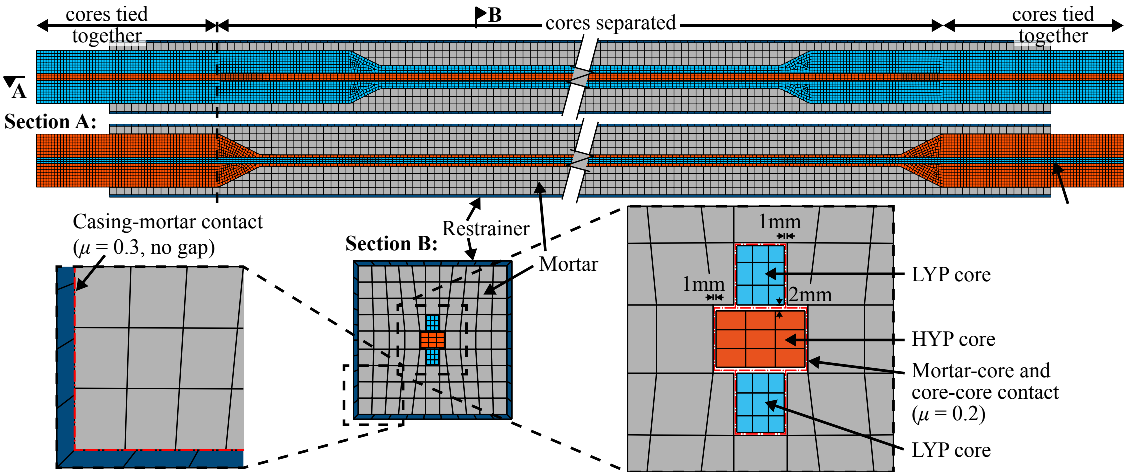

Fig. 13. Finite element model.

ε_y, f_u, ε_u) (Table 2), although these remained nominally elastic. The mortar was modelled using a Concrete Damaged Plasticity model following [23] (Popovics/Saenz compressive stress-strain curve with strength $f_{ck} = 44$ MPa at strain $\varepsilon_c = 0.24\%$, 20° dilation angle, a compression damage parameter of 0.3, and Cornellissen tensile stress-crack width curve with strength $f_t = 3.8$ MPa and fracture energy $G_f = 53$ N/m).

As the cores are subjected to cyclic yielding, the "combined hardening" model was adopted. The constitutive material model was initially calibrated to the monotonic LYP225 and SA440B coupon tests and cyclic data from Ono and Sato [24], and then adjusted through trial and error to match the experimental results. Emphasis was placed on matching the stresses up to 2% strain, cyclic tangent stiffness, ultimate strain and isotropic hardening, which control the global δ_{BRB} - N_{BRB} hysteresis, higher-mode buckling wavelength, necking and strain ratcheting, respectively. Table 4 lists the calibrated parameters, which the Abaqus documentation describes in detail [22].

4.2. Numerical results

The BRB force-displacement and core stress-strain hysteresis are compared to the experimental results for the ascending cycles, stable fatigue cycles (#1–20) and deteriorating fatigue cycles (#21–25) in Fig. 14. The final fatigue cycle (#26) where fracture occurred is not included. The numerical results are in good agreement, matching the yielding and hardening characteristics of both cores. However, pinching was less pronounced over the final cycles, reasons for which will be discussed at the end of this section.

The energy dissipation characteristics of the LYP and HYP cores are almost identical to the experimental results, as shown in Fig. 15a. Although the strain gauges were not functioning during most of the fatigue protocol, the numerical results indicate that the equivalent viscous damping contributions of both cores remained stable until severe higher-mode buckling was observed, which occurred slightly earlier in the finite element analysis.

The compressive overstrength factor (β) is compared in Fig. 15b. The numerical results reproduced the β value of less than 1.0 during the small amplitude cycles, which is attributed to the strain relaxation phenomena discussed earlier (Fig. 9b). Although the numerical analysis indicates a slightly smaller β during some of the initial cycles, the deviation is within the expected uncertainty that arises from the random variation of the higher-mode buckling wavecrest widths. The compressive overstrength then increased to $\beta = 1.06$ at $\varepsilon_L = 1.5\%$ and remained stable throughout the fatigue cycles, the same as observed in the experiment.

Table 4
Calibrated constitutive material properties.

Steel grade	E GPA	σ_0 MPa	C_1/γ_1 MPa	γ_1 –	C_2/γ_2 MPa	γ_2 –	C_3/γ_3 MPa	γ_3 –	Q_∞ MPa	b –
LY225	205	170	55	700	130	9	250	1	60	5
SA440B	180	365	140	350	180	22	180	1	–	–

The primary purpose of the numerical analysis was to identify the cause of the large-amplitude higher-mode buckling, which eventually led to pinching and premature fracture. Fig. 16 shows the plastic strain distribution and buckled core shape when severe higher-mode buckling was first observed.

The numerical results suggest that the HYP core controlled the final higher-mode buckling wavelength and shape, as these did not significantly change along the LYP elastic zone, where only the HYP core is undergoing plastic higher-mode buckling. Conversely, the LYP cores controlled the higher-mode buckling wavelength during the small amplitude cycles due to the larger strain demands, and appeared to be converging to the final observed wavelength. This suggests that LY225 and SA440B have similar higher-mode buckling wavelengths, despite the large difference in steel grade.

Large-amplitude higher-mode buckling only occurred after mortar at the weak axis faces of the HYP core was crushed. The bearing stresses at these locations exceeded the 44 MPa mortar compressive strength during the first cycle at $\varepsilon_L = 1.5\%$, and subsequent crushing concentrated near the ends of the LYP core yield lengths, matching the observed fracture location. The large higher-mode buckling amplitude resulted in severe bending strain demands at the HYP core wave troughs over the final cycles, reversing between $+6\%$ (tensile) and -18% (compression) equivalent plastic strains and reaching a cumulative equivalent plastic strain of PEEQ = 290%. Finally, although the large-amplitude higher-mode buckling did cause slight bulging near the ends of the LYP core yield lengths, this was restrained by the SHS steel tube and had a negligible effect on the axial force-displacement response, the same as observed in the experiment.

While the higher-mode buckling amplitude gradually increased as the mortar experienced plastic strains and compressive damage (softening of the unloading modulus), the finite element mesh was not able to capture the movement of the loose mortar grains. This likely affected the mortar divot depth and pinching over the final deteriorating cycles, as migrating the crushed mortar grains from the bearing faces to between the HYP and LYP cores at the wave troughs (Fig. 16) would further increase the higher-mode buckling amplitude of the HYP core. Nevertheless, the numerical results indicate that mortar crushing at the narrow contact zones along the weak axis faces of the HYP core was responsible for the large-amplitude higher-mode buckling and

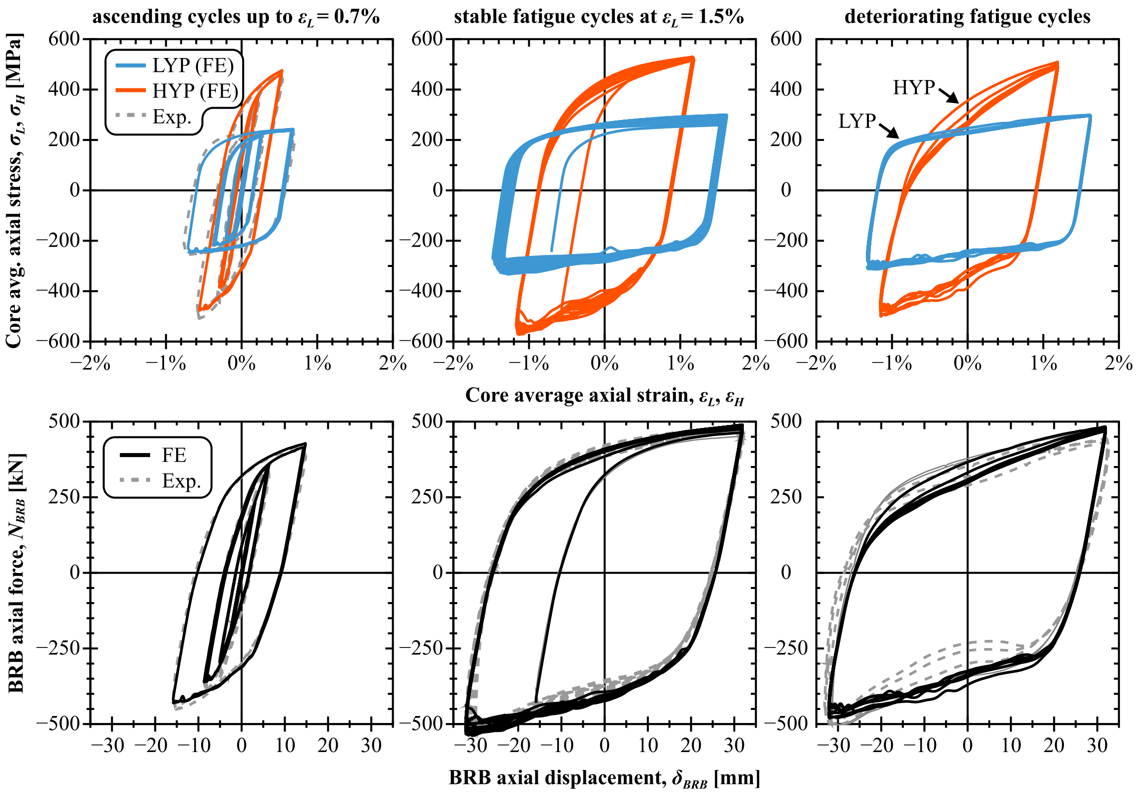

Fig. 14. Cyclic hysteresis.

premature fracture. Reducing the debonding gap between the LYP and HYP cores, and widening the HYP core in a full-scale device would reduce the bearing stress, and so revising these details should prevent mortar crushing and severe higher-mode buckling, further improving the fatigue performance.

5. Discussion

5.1. Multistage behavior

The primary objective of experimentally validating the multistage behavior was achieved. The displacement and force at first yield closely matched the estimated values of $N_{y,L} = 262$kN and $\delta_{y,L} = 2.9$, while the gross yield strength of $N_y = 384$kN developed at displacements corresponding to a 0.2% strain offset of the HYP core, as predicted. Furthermore, the SA440B HYP core provided a post-yield stiffness ratio of 0.04 at a ductility of $\delta_{BRB}/\delta_y = 7$, approximately twice that of conventional BRBs [25]. This indicates that a trilinear backbone curve calculated from the nominal yield strengths and strains is appropriate for numerical archetype frame studies, and that a relatively large post-yield stiffness after yielding the HYP core may be justified.

The multistage behavior was evident in the improved energy dissipation at small displacements, with early yielding of the LYP cores producing 10–20% overall equivalent viscous damping at $\varepsilon_L = 0.2$–0.4%. This supplementary hysteretic damping is expected to significantly improve the system performance, given that the greatest incremental benefit of increased energy dissipation occurs for small damping ratios [1]. This confirms that the device is capable of providing substantial energy dissipation and enhanced post-yield stiffness during small and moderate earthquakes.

5.2. Core configuration and debonding gap

The test specimen employed an unusual decoupled cruciform configuration, and this test highlighted that the debonding gap and HYP core detailing could be improved. Although the clearance must be large

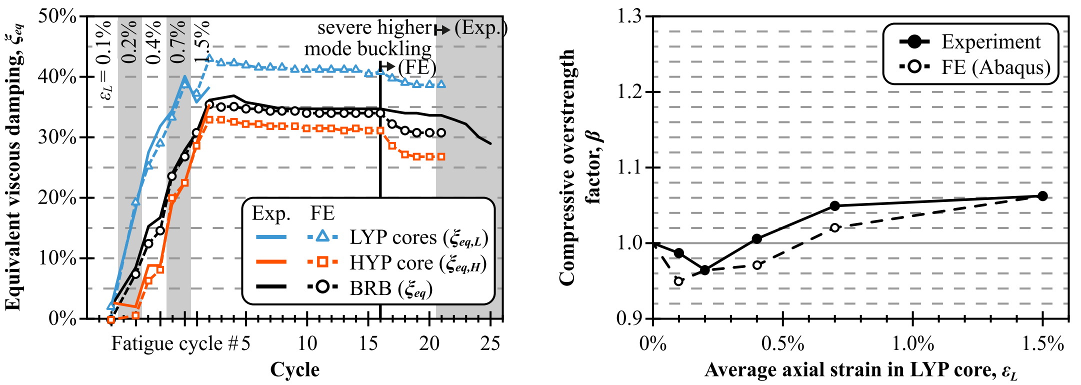

a) Equivalent viscous damping

b) Hysteretic energy dissipation

Fig. 15. Cyclic response.

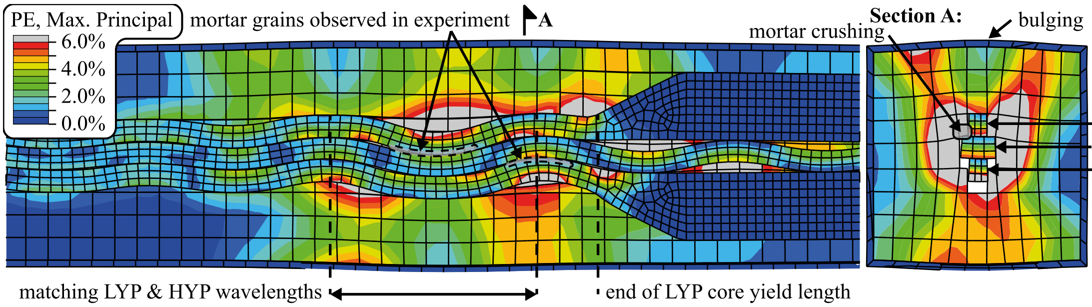

Fig. 16. Plastic strain distribution at 16th fatigue cycle.

enough to accommodate Poisson expansion while accounting for fabrication tolerances, excessive gaps give rise to geometric strain relaxation and increase the lateral thrust, resulting in larger compressive forces and potentially bulging. In the test specimen, the gaps between and outside the cores acted cumulatively, and so wrapping the cores individually aggravated an already large effective clearance.

The narrow HYP core ($W_{c,H} = 30$ mm) resulted in just a 6 mm bearing width on either side of the perpendicular LYP cores ($t_{c,L} = 16$ mm), crushing the mortar during the $\varepsilon_L = 1.5\%$ cycles. Reducing the gap between the HYP and LYP cores, while increasing the HYP core width could keep the bearing stresses below the mortar's compressive strength. Regardless, a high strength mortar is advisable when adopting the proposed decoupled core configuration. While these detailing changes are subject to future study, the severe higher-mode buckling that led to a premature fracture in this test appears surmountable.

5.3. Higher-mode buckling and compressive overstrength

The recorded compressive overstrength factor was only $\beta = 1.06$ at $\varepsilon_L = 1.5\%$, an excellent result. However, it may not be appropriate to extrapolate this value to full-scale MS-BRBs, as the large debonding gap employed in the test specimen resulted in significant compressive strain relaxation (Fig. 9b). Resolving the mortar crushing and large debonding gap (Section 5.2) would increase β to closer to 1.0 at small strains, but it is not apparent if this would have a net beneficial or adverse effect at large strains, as a smaller amplitude also reduces the lateral thrust and friction forces. Nevertheless, splitting the core into separate rectangles does not appear to have an adverse effect on the compressive overstrength. Note that further investigation would be required before extrapolating this conclusion to longer braces, where friction effects are more pronounced.

5.4. Fatigue and displacement demands

The fatigue performance was satisfactory, as the test specimen fractured in tension and exceeded three times the AISC 341-16 cumulative inelastic deformation criteria. This suggests that the device is capable of withstanding multiple design level events, with reserve capacity to spare and potential for further improvements if mortar crushing is prevented (Section 5.2). Avoiding the need to replace MS-BRBs after yielding in an earthquake is essential, as the primary purpose of the proposed device is to improve the post-earthquake repair/replace decision.

While the proposed device requires a short LYP core yield length, the enhanced energy dissipation and greater stiffness of MS-BRBs slightly reduces the peak displacements [10–12,15], offsetting the increase in strain demands to a certain extent. However, AISC 341 penalizes extremely short yield lengths by imposing a minimum 2% drift for qualification tests (§K3.4c [19]), and so yield length ratios significantly shorter than the tested $L_{y,L}/L_{wp} = 0.44$ may have difficulty meeting the multi-event fatigue criteria. Therefore, it is proposed to set $L_{y,L}/L_{wp} > 0.4$ as a practical limit when designing the yield drift differential (Eq. (9)).

5.5. Comparison to conventional BRBs

While the component level response suggests that the proposed device is capable of achieving the intended performance, it is illustrative to compare the drawbacks and benefits of MS-BRBs to conventional BRBs, particularly with regard to the suitable project types and fabrication.

Performance reasons related to the narrow HYP cores (Section 5.2) and required core yield lengths (Section 5.4) may render the device less suitable for small ($N_y < 800$ kN) or short ($L_{wp} < 4$ m) applications. This is to avoid mortar crushing and ensure that a reasonable yield length differential is feasible, while limiting the LYP strain demand. Also, it would be redundant to use MS-BRBs in dual BRB-moment frames, which are typically required in tall buildings, as the moment frame fulfills the same purpose as the HYP core. Conversely, the device may be particularly well suited to low-to-midrise buildings where the client desires a resilient and cost-effective design. Multistory commercial and residential buildings are attractive candidates, as well as those requiring long BRBs, such as warehouses and spatial structures.

In terms of fabrication, multiple core materials must be sourced, which while unlikely to be a problem for LYP cores using LY225 or A36, may be a challenge for the HYP core unless the supplier regularly uses ductile high strength steels for other applications. Although the core configuration requires multiple plates, which increases the total plate cutting length, the cores do not require full-length longitudinal welds. The fabrication procedures are otherwise identical to conventional mortar-filled steel-tube BRBs, and were easily accommodated in the normal production schedule of the BRB fabricator used for this test.

6. Conclusions

A new multistage BRB featuring two short LYP cores parallel to a longer HYP core was proposed and tested, drawing the following conclusions:

- A trilinear backbone curve calculated from the nominal core strengths was validated by testing a MS-BRB specimen with $N_y = 384$ kN and $\delta_{y,H}/\delta_{y,L} = 2.2$ up to a LYP core strain of $\varepsilon_L = 1.5\%$.
- Early yielding of the LYP cores produced 10–20% equivalent damping prior to yielding the HYP core. Kinematic hardening of the SA440B HYP core subsequently provided a post-yield stiffness ratio of 0.04.
- Three times the AISC 341-16 cumulative inelastic deformation criteria was achieved ($CID_{AISC} = 652$, or $CID_{LYP} = 1054$ if normalized by $\delta_{y,L}$). Tensile fracture occurred after 26 fatigue cycles at $\varepsilon_L = 1.5\%$ with a LCF damage index of $D_{LCF} = 55\%$, as severe higher-mode buckling caused a premature fracture.
- Core higher-mode buckling was investigated using a 3D Abaqus/

Explicit model, indicating that the narrow HYP core ($W_{c,H} = 30$ mm) locally crushed the mortar on either side of the LYP cores ($t_{c,L} = 16$ mm). This may be mitigated by increasing the HYP core width, potentially controlling the minimum practical size.

This test confirmed the feasibility of the proposed decoupled core configuration and achieved the intended multistage behavior, offering engineers a new device to reduce residual drifts in simply supported BRBFs.

CRediT authorship contribution statement

Ben Sitler: Conceptualization, Methodology, Investigation, Formal analysis, Writing - original draft. **Toru Takeuchi:** Supervision, Conceptualization, Writing - review & editing. **Ryota Matsui:** Project administration, Methodology. **Masao Terashima:** Resources, Funding acquisition. **Yuki Terazawa:** Investigation.

Appendix A. Supplementary material

Supplementary data to this article can be found online at https://doi.org/10.1016/j.engstruct.2020.110482.

References

[1] Takeuchi T, Wada A. Buckling-restrained braces and applications. Jpn Soc Seism Isolat 2017.

[2] MacRae G, Kimura Y, Roeder C. Effect of column stiffness on braced frame seismic behaviour. J Struct Eng ASCE 2004;130:381–91. https://doi.org/10.1061/(ASCE)0733-9445(2004)130:3(381).

[3] Zaruma S, Fahnestock L. Assessment of design parameters influencing seismic collapse performance of buckling-restrained braced frames. Soil Dyn Earthq Eng 2018;113:35–46. https://doi.org/10.1016/j.soildyn.2018.05.021.

[4] Kiggins S, Uang C. Reducing residual drift of buckling-restrained braced frames as a dual system. Eng Struct 2006;28:1525–32.

[5] Wada A, Connor J, Kawai H, Iwata M, Watanabe A. Damage tolerant structure. 5th US-Japan Workshop on the Improvement of Building Structural Design and Construction Practices; 1992.

[6] Takeuchi T, Chen X, Matsui R. Seismic performance of controlled spine frames with energy-dissipating members. J Constr Steel Res 2015;114:51–65. https://doi.org/10.1016/j.jcsr.2015.07.002.

[7] Miller D, Fahnestock L, Eatherton M. Development and experimental validation of a nickel-titanium shape memory alloy self-centering buckling-restrained brace. Eng Struct 2012;40:288–98. https://doi.org/10.1016/j.engstruct.2012.02.037.

[8] Yamamoto M, Sone T. Damping systems that are effective over a wide range of displacement amplitudes using metallic yielding component and viscoelastic damper in series. Earthq Eng Struct Dyn 2014;43:2097–114. https://doi.org/10.1002/eqe.2438.

[9] Saeki E. Hysteresis characteristics of steels and buckling restrained unbonded braces. Doctoral Thesis, Tokyo Institute of Technology; 1997 [in Japanese].

[10] Atlayan O, Charney F. Hybrid buckling-restrained braced frames. J Constr Steel Res 2014;96:95–105.

[11] Jia LJ, Li RW, Xiang P, Zhou DY, Dong Y. Resilient steel frames installed with self-centering dual-steel buckling-restrained brace. J Constr Steel Res 2018;149:95–104. https://doi.org/10.1016/j.jcsr.2018.07.001.

[12] Hoveidae N. Numerical investigation of seismic response of hybrid buckling restrained braced frames. Period Polytech Civ Eng 2019;63:130–40. https://doi.org/10.3311/PPci.12040.

[13] Barbagallo F, Bosco M, Marino E, Rossi P. Achieving a more effective concentric braced frame by the double stage yield BRB. Eng Struct 2019;186:484–97. https://doi.org/10.1016/j.engstruct.2019.02.028.

[14] Architectural Institute of Japan. Recommended provisions for seismic damping systems applied to steel structures; 2014 [in Japanese].

[15] Sitler B, Takeuchi T. Effect of steel grade and core yield length in multistage buckling-restrained braces subjected to mainshock-aftershock sequences. Pacific Struct Steel Conf 2019.

[16] Li GQ, Sun YZ, Jiang J, Sun FF, Ji C. Experimental study on two-level yielding buckling-restrained braces. J Constr Steel Res 2019;159:260–9. https://doi.org/10.1016/j.jcsr.2019.04.042.

[17] Sun J, Pan P, Wang H. Development and experimental validation of an assembled steel double-stage yield buckling restrained brace. J Constr Steel Res 2018;145:330–40. https://doi.org/10.1016/j.jcsr.2018.03.003.

[18] Nippon Steel Engineering. Unbonded brace catalogue; 2016 [in Japanese].

[19] American Institute of Steel Construction. Seismic provisions for structural steel buildings. ANSI/AISC 341-16; 2016.

[20] Shibata A. Dynamic analysis of earthquake resistant structures. Sendai: Tohoku University Press; 2010.

[21] Yoshikawa H, Nishimoto K, Konishi H, Watanabe A. Fatigue properties of unbonded braces and u-shaped steel dampers. Nippon Steel Engineering Technical Report 2010;11:84–91. [in Japanese].

[22] Smith M. ABAQUS/Explicit User's Manual, Version 2017. Simulia; 2017.

[23] Nguyen N, Whittaker A. Numerical modelling of steel-plate concrete composite shear walls. Eng Struct 2017;150:1–11. https://doi.org/10.1016/j.engstruct.2017.06.030.

[24] Ono T, Sato A. Modeling of stress-strain relationships of metallic materials. J Struct Constr Eng AIJ 2000;532:177–84. https://doi.org/10.3130/aijs.65.177_2. [in Japanese].

[25] Black C, Makris N, Aiken I. Component testing, seismic evaluation and characterization of buckling-restrained braces. J Struct Eng ASCE 2004;130:880–94. https://doi.org/10.1061/(ASCE)0733-9445(2004)130:6(880).